INNER MASS DETERMINATION OF A MASSIVE GALAXY CLUSTER ABELL 1689[1]

Kristen P. Wu

International Bilingual School at Hsinchu Science Park

Advisor

Tzihong Chiueh, Phd.

Department of Physics

College of Science

National Taiwan University

August 31, 2011

ABSTRACT

We analyzed the strong lensing effects of galaxy cluster Abell 1689 to determine its inner mass distribution. Abell 1689 is the most massive galaxy cluster known, and with the help of the Hubble Space Telescope, it can provide more than 100 multiple images for our purpose, which is to be examined against the theoretically motivated Narravo-Frenk-White (NFW) model. Using the Pixelens software, we constructed the mass density profile of Abell 1689. From our results, we found that a modified core model with a small single isothermal sphere agrees much better with the data than the commonly-accepted NFW model does. Through our work, we also identified the limitations of Pixelens.

Contents

---

[1] Based from observations from the NASA/ESA Hubble Space Telescope

1. INTRODUCTION

Albert Einstein once predicted that gravity warped space and therefore distorted light. When the Advanced Camera for Surveys (ACS) on NASA's Hubble Space Telescope (HST) looked into the center of Abell 1689 in 2003, astronomers were able to view this giant galaxy cluster with greater clarity and sensitivity than before.

Abell 1689 is a z=0.18 galaxy cluster located in the constellation of Virgo. It has long been an object of great interest due to its identity as one of the most massive known galaxy clusters. The more immense a galaxy cluster, the larger the effects of gravitational lensing. The gravity of Abell 1689's trillion stars and dark matter acts like a two-million-light-year-wide gravitational lens, bending and magnifying the light of galaxies behind it. The most impressive lensing cluster yet found, Abell 1689 is "an immense jigsaw puzzle for Hubble astronomers to spend months untangling."[2]

Gravitational lensing occurs when a very massive and dense object such as a galaxy cluster is in the direct path of another object's light from its source to us observers. The light is then bent around the cluster, according to general relativity. Lensing is used to measure mass and mass distribution, since lensing is equally sensitive to both dark and luminous matter, and to matter in equilibrium or far out of it equilibrium [1]. Therefore, lensing is the ideal tool to measure the total mass of astronomical bodies, both dark and luminous. With HST imaging and knowledge of multiple image systems in some lensing clusters, detailed mass maps have been obtained along with very precise mass estimates.

Using the new non-parametric method implemented by the Pixelens software (a more detailed explanation can be found in Section 2.2), we reconstructed the projected mass distribution in galaxy cluster A1689. Several prior works also made similar attempts. We then compare our result with these others.

2. LENS EQUATION

The theory of General Relativity predicts that light rays bend when they pass near a massive body. Gravitational lensing is based on this theory. Light is deflected by a point-like mass *M* with an angle α

$$\alpha = \frac{4GM}{c^2 b},\qquad(2.1)$$

---

[2] See http://hubblesite.org/newscenter/archive/releases/2003/01/text/

where b represents the impact parameter of light rays. A more general formula is obtained by dividing the system into a number of pointlike masses $M_i\left(\vec{\xi}_i', r_3\right)$ and then summing up the contributions from each small mass piece

$$\vec{\alpha}\left(\vec{\xi}\right) = \sum_i \frac{4G}{c^2} \Sigma_i\left(\vec{\xi}_i', r_3\right) \frac{\vec{\xi} - \vec{\xi}_i'}{\left|\vec{\xi} - \vec{\xi}_i'\right|^2}, \qquad (2.2)$$

where $\vec{\xi} - \vec{\xi}_i'$ is the impact vector of light rays from the surface mass unit $\Sigma_i \equiv M_i\left(\xi_i, r_3 = 0\right)$. The integral form of the formula is

$$\vec{\alpha}\left(\vec{\xi}\right) = \frac{4G}{c^2} \int \Sigma_i\left(\vec{\xi}'\right) \frac{\vec{\xi} - \vec{\xi}'}{\left|\vec{\xi} - \vec{\xi}'\right|^2} d^2\vec{\xi}'. \qquad (2.3)$$

Here $\Sigma\left(\vec{\xi}'\right)$ is the surface mass density at position $\vec{\xi}_i'$ obtained by projecting all the lens mass along the line of sight r_3 onto a lens sheet. That is, $\Sigma_i\left(\vec{\xi}_i'\right) = \int \rho\left(\vec{\xi}_i', r_3\right) dr_3$, in which $\rho\left(\vec{\xi}_i', r_3\right)$ is the volume mass density.
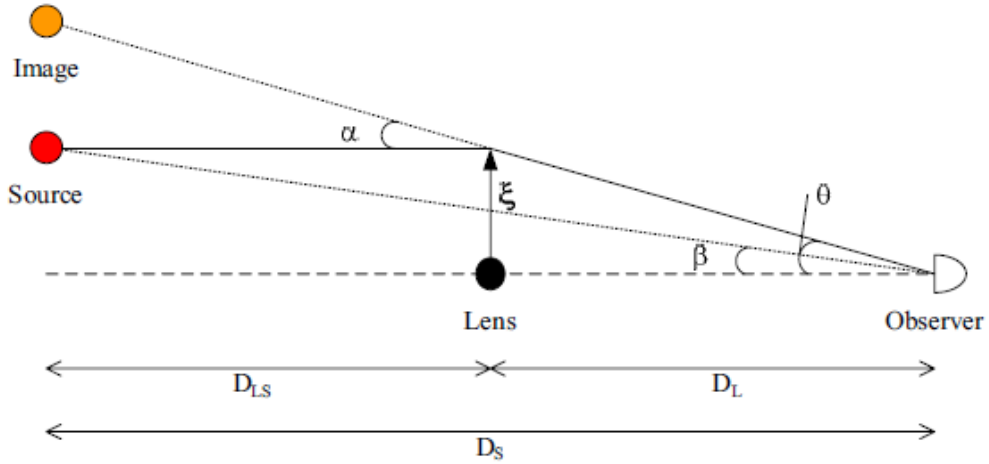

Figure 1. Diagram of a typical gravitational lens system.

From Figure 1, we can see that a light ray from the source at distance D_S is deflected by the gravitational lens at a distance D_L from the observer by the angle $\vec{\alpha}$, so that it is observed at the angle $\vec{\theta}$. The figure also shows the geometric condition that

$$D_{LS}\vec{\alpha} = D_S\vec{\theta} - D_S\vec{\beta}. \qquad (2.4)$$

3

From equation 2.3, the deflection angle $\vec{\alpha}$ can be written as the gradient of the two-dimensional deflection potential ψ

$$\vec{\theta} - \vec{\beta} = \frac{D_{LS}}{D_S}\vec{\alpha} \equiv \nabla_\theta \psi\left(\vec{\theta}\right). \tag{2.5}$$

The identity $\nabla_\theta \ln\left|\vec{\theta}\right| = \vec{\theta}/\left|\vec{\theta}\right|^2$, valid for any two-dimensional vector $\vec{\theta}$, shows that the potential can be written

$$\psi\left(\vec{\theta}\right) = \frac{4G}{c^2}\int \frac{D_L D_{LS}}{D_S}\Sigma\left(\vec{\theta}'\right)\ln\left|\vec{\theta} - \vec{\theta}'\right| d^2\vec{\theta}', \tag{2.6}$$

where we introduce angular coordinates by

$$\vec{\xi} = D_S\vec{\beta} = D_L\vec{\theta}' \quad \text{and} \quad \vec{\xi}' = D_L\vec{\theta}'. \tag{2.7}$$

D_S, D_L, and D_{LS} are all angular diameter distances (Appendix A). Using the identity $\nabla_\theta^2 \ln\left|\vec{\theta} - \vec{\theta}'\right| = 2\pi\delta_{2D}\left(\vec{\theta} - \vec{\theta}'\right)$, where δ_{2D} is the two-dimensional Dirac delta function. We obtain from Equation 2.6 that

$$\nabla_\theta^2 \psi = 2\frac{\Sigma}{\Sigma_c} \equiv 2\kappa, \tag{2.8}$$

In which the quantity Σ_c is called the critical surface mass density defined as

$$\Sigma_c = \frac{c^2}{4\pi G}\frac{D_S}{D_L D_{LS}}. \tag{2.9}$$
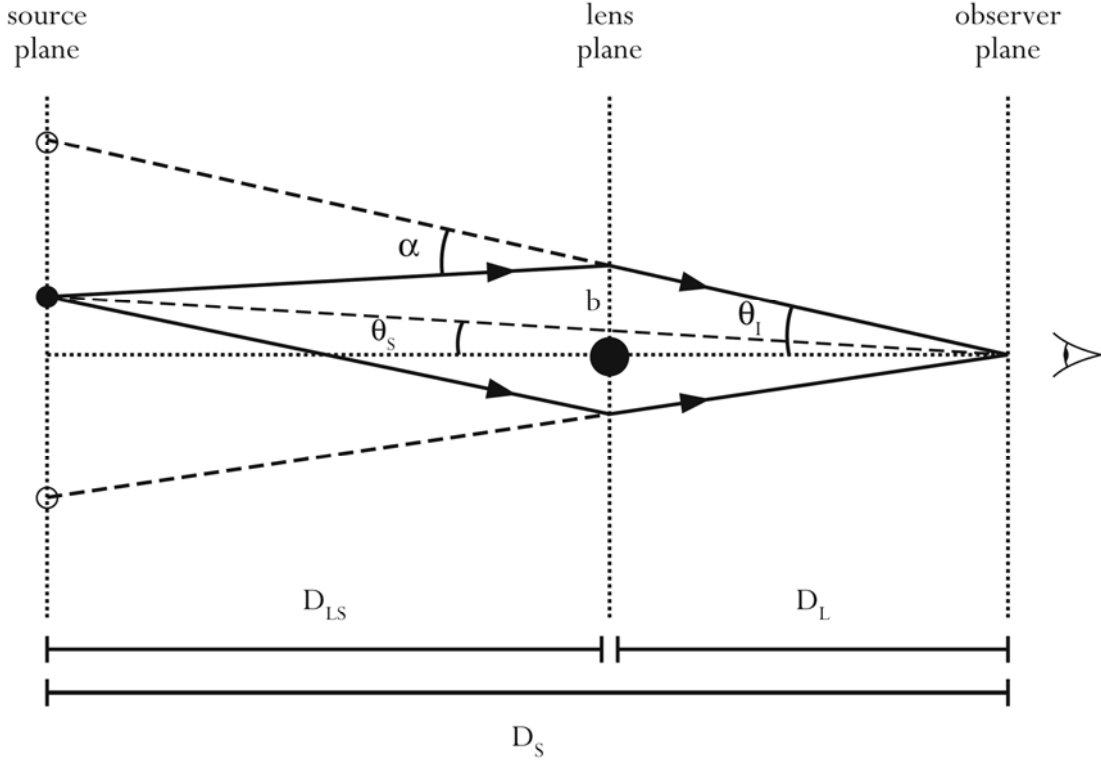

4

Figure 2. Two images arrive at the observer from the same source. The parity and arrival time (further explained in Section 3), can also be observed in this diagram.

For our research, we made use of multiple image systems to extract the cluster mass information. One may identify multiple images by spectroscopic features, such as identical spectral lines and line strengths. Single images are not useful because we do not know their exact original shapes and luminosity, and therefore do not know how they are affected by the lens. In gravitational lensing, two or more images can arrive at the same observer from the same source. When two images have same spectroscopic features they are most likely coming from the same source. The situation is drawn in Figure 2.
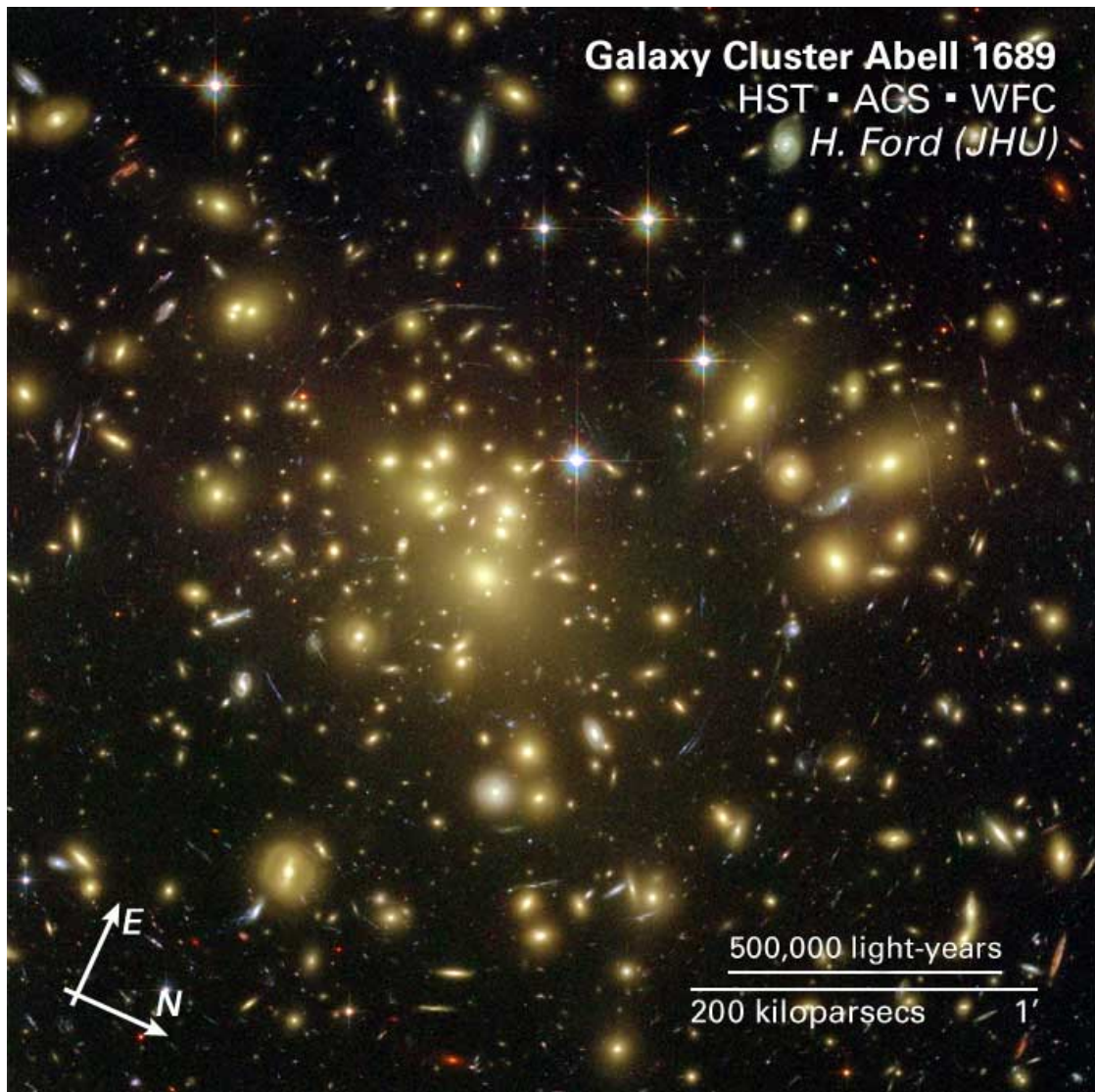

Figure 3. Four-color image of A1689 taken by Hubble Space Telescope ACS/WFC instruments in 2002 with filters F475W (*g*), F625W (*r*), F775W (*i*), F850LP (*z*).

3. METHODOLOGY

3.1 Collecting and Organizing Data

In order to study this cluster, we extracted a composite color image from the Hubble Space Telescope's public release (shown above in Figure 3.). The filters used were F475W (*g*), F625W (*r*), F775W (*i*), F850LP (*z*), where the central wavelength in nanometers is encoded in the filter

First of all, we needed to know the positions of all image in the multiple image system. We consulted previous works on gravitational lensing in A1689. The lensing images we used are from the multiply imaged systems provided by Limousin et al. (2007) (see Table I) [2]. The coordinates were given so that "N" would point to the right and "E" would point up (see Figure 3). The spectroscopic and estimated redshifts were also given by Limousin et al. (2007), but we only used spectroscopic redshifts.

ID	R.A.	Decl.	F775W	z_{phot}[a]	z_{model}[b]	z_{spec}[c]
1.1	13 11 26.447	−1 19 56.68	23.44	$3.03^{+0.53}_{-0.53}$	...	3.0
1.2	13 11 26.287	−1 19 59.69	23.69	$3.04^{+0.53}_{-0.53}$	...	...
1.3	13 11 29.771	−1 21 07.34	24.52	$3.27^{+0.56}_{-0.56}$	...	3.0
1.4	13 11 33.055	−1 20 27.31	24.16	$2.94^{+0.52}_{-0.52}$	...	...
1.5	13 11 31.933	−1 20 05.69	24.62	$3.35^{+0.57}_{-0.57}$	...	...
1.6	13 11 29.851	−1 20 38.32	25.82	$1.06^{+1.91}_{-0.27}$	...	...
2.1	13 11 26.528	−1 19 55.08	23.37	$2.62^{+0.47}_{-0.48}$	...	2.5
2.2	13 11 32.961	−1 20 25.31	24.18	$2.57^{+0.47}_{-0.47}$	...	...
2.3	13 11 31.973	−1 20 06.89	24.36	$2.64^{+0.48}_{-0.48}$	...	...
2.4	13 11 29.811	−1 21 05.94	24.48	$2.36^{+0.44}_{-0.44}$	...	2.5
2.5	13 11 29.878	−1 20 39.32	25.63	$1.59^{+0.86}_{-0.34}$	...	...
3.1	13 11 32.043	−1 20 27.41	26.65	$5.48^{+0.85}_{-0.85}$	3.25 ±1.47	...
3.2	13 11 32.174	−1 20 33.31	26.85	$5.45^{+0.85}_{-0.85}$	...	...
3.3	13 11 31.680	−1 20 55.88	...	...	...	...
4.1	13 11 32.174	−1 20 57.33	24.62	$1.06^{+0.27}_{-0.27}$	...	1.1
4.2	13 11 30.518	−1 21 11.94	23.91	$1.32^{+0.30}_{-0.31}$	...	...
4.3	13 11 30.759	−1 20 07.89	25.12	$1.47^{+0.32}_{-0.33}$	...	...
4.4	13 11 26.287	−1 20 35.11	24.67	$1.33^{+0.31}_{-0.31}$	...	...
4.5	13 11 29.838	−1 20 29.11	...	...	...	...
5.1	13 11 29.064	−1 20 48.33	24.42	$3.29^{+0.56}_{-0.56}$	...	2.6
5.2	13 11 29.224	−1 20 43.92	24.92	$3.16^{+0.55}_{-0.55}$	...	...
5.3	13 11 34.109	−1 20 20.90	25.26	$2.15^{+0.67}_{-0.41}$	...	2.6
6.1	13 11 30.759	−1 19 37.87	23.61	$1.22^{+0.29}_{-0.29}$	...	1.1
6.2	13 11 33.335	−1 20 12.10	23.85	$1.31^{+0.30}_{-0.30}$	...	1.1
6.3	13 11 32.734	−1 19 54.28	23.02	$0.94^{+0.26}_{-0.25}$	...	...
6.4	13 11 32.481	−1 19 58.69	24.00	$1.09^{+0.27}_{-0.27}$	...	...
7.1	13 11 25.446	−1 20 51.53	23.31	$4.92^{+0.78}_{-0.78}$	...	4.8
7.2	13 11 30.679	−1 20 13.70	24.19	$5.20^{+0.81}_{-0.81}$	...	4.8
7.3	13 11 29.824	−1 20 24.71	28.23	$0.77^{+4.01}_{-0.23}$	...	...
8.1	13 11 32.300	−1 20 50.78	24.54	$2.63^{+0.48}_{-0.48}$	2.30±0.21	...
8.2	13 11 31.393	−1 21 05.59	24.31	$2.77^{+0.50}_{-0.50}$	...	...
8.3	13 11 31.500	−1 20 13.95	25.71	$2.75^{+0.49}_{-0.89}$	...	...
8.4	13 11 25.520	−1 20 20.15	23.97	$0.70^{+0.22}_{-0.22}$	...	...
8.5	13 11 30.325	−1 20 30.46	27.42	$0.77^{+2.53}_{-0.23}$	...	...
9.1	13 11 30.298	−1 19 48.33	25.92	$4.97^{+0.78}_{-0.78}$	2.69±0.27	...
9.2	13 11 33.515	−1 20 50.38	27.53	$1.06^{+0.27}_{-0.27}$	...	...
9.3	13 11 28.723	−1 21 15.60	25.72	$5.16^{+0.81}_{-0.81}$	...	...
9.4	13 11 26.267	−1 20 26.56	27.15	$5.17^{+0.81}_{-0.81}$	...	...
10.1	13 11 33.976	−1 20 50.93	23.66	$1.75^{+0.74}_{-0.36}$	...	1.8
10.2	13 11 28.049	−1 20 12.30	23.30	$1.54^{+0.33}_{-0.33}$	...	...
10.3	13 11 29.317	−1 20 27.71	25.15	$2.57^{+0.47}_{-0.63}$	...	...
11.1	13 11 33.333	−1 21 06.74	24.03	$2.91^{+0.51}_{-0.51}$	...	2.5
11.2	13 11 29.064	−1 20 01.09	23.36	$2.87^{+0.51}_{-0.51}$	...	...
11.3	13 11 29.491	−1 20 26.31	26.78	$1.58^{0.73}_{-0.52}$	...	...
12.2	13 11 27.355	−1 20 54.73	24.30	$1.99^{+0.39}_{-0.39}$	...	1.8
12.3	13 11 27.208	−1 20 51.53	23.97	$1.99^{+0.39}_{-0.39}$	...	...
13.1	13 11 32.821	−1 19 24.11	24.10	$1.02^{+0.28}_{-0.27}$	1.5±0.5	...
13.2	13 11 32.994	−1 19 25.51	23.68	$0.72^{+0.23}_{-0.23}$	...	...
13.3	13 11 33.408	−1 19 31.11	24.12	$1.10^{+0.28}_{-0.28}$	...	...
14.1	13 11 29.024	−1 21 41.77	24.98	$3.37^{+0.57}_{-0.82}$	...	3.4
14.2	13 11 29.454	−1 21 42.67	25.99	$3.64^{+0.61}_{-0.61}$	...	...
15.1	13 11 28.083	−1 20 14.75	25.69	$1.99^{+0.39}_{-0.39}$	...	1.8
15.2	13 11 34.076	−1 20 51.38	25.79	$2.00^{+0.39}_{-0.39}$	...	...
15.3	13 11 29.244	−1 20 27.36	27.16	$1.97^{+0.39}_{-0.43}$	...	...
16.1	13 11 27.989	−1 20 24.96	23.68	$1.81^{+0.37}_{-0.37}$	1.76±0.16	...
16.2	13 11 28.923	−1 20 28.36	25.06	$2.26^{+0.43}_{-0.43}$	...	...
16.3	13 11 34.396	−1 20 46.37	25.35	$1.80^{+0.71}_{-0.37}$	...	...
17.1	13 11 30.655	−1 20 24.76	24.19	$2.74^{+0.49}_{-0.49}$	...	...
17.2	13 11 30.388	−1 20 27.56	25.11	$2.02^{+0.40}_{-0.40}$	...	...
17.3	13 11 24.983	−1 20 41.37	24.31	$2.25^{+0.43}_{-0.43}$	...	2.6
18.1	13 11 28.243	−1 20 09.34	25.00	$2.56^{+0.47}_{-0.47}$	...	1.8
18.2	13 11 33.809	−1 20 54.58	...	...	...	...
18.3	13 11 29.364	−1 20 27.16	26.78	$1.58^{+0.73}_{-0.52}$	...	...
19.1	13 11 31.633	−1 20 22.56	24.83	$1.72^{+0.36}_{-0.36}$	...	...

ID	R.A.	Decl.	F775W	z_{phot}[a]	z_{model}[b]	z_{spec}[c]
19.2	13 11 25.253	−1 20 19.75	25.23	$2.74^{+0.49}_{-0.49}$	...	...
19.3	13 11 31.953	−1 20 59.18	25.88	$1.57^{+0.34}_{-0.34}$	...	...
19.4	13 11 32.033	−1 20 57.38	24.76	$2.58^{+0.47}_{-0.47}$	...	2.6
19.5	13 11 30.218	−1 20 33.76	27.94	$4.54^{+1.66}_{-0.73}$	...	...
21.1	13 11 31.019	−1 20 45.77	25.15	$1.79^{+0.37}_{-0.37}$	1.91±0.19	...
21.2	13 11 30.792	−1 20 44.57	26.70	$1.59^{+0.34}_{-0.34}$	...	...
21.3	13 11 25.253	−1 20 10.95	25.59	$1.78^{+0.36}_{-0.36}$	...	...
22.1	13 11 29.694	−1 20 08.54	23.66	$1.99^{+0.39}_{-0.39}$	...	1.7
22.2	13 11 29.614	−1 20 23.56	25.49	$1.99^{+0.59}_{-0.39}$	...	...
22.3	13 11 32.404	−1 21 16.00	23.27	$1.96^{+0.39}_{-0.39}$	...	...
23.1	13 11 29.524	−1 20 09.74	24.63	$2.03^{+0.40}_{-0.40}$	1.78±0.20	...
23.2	13 11 29.551	−1 20 22.76	25.99	$1.99^{+0.62}_{-0.39}$	...	...
23.3	13 11 32.661	−1 21 15.20	24.72	$2.00^{+0.39}_{-0.39}$	...	...
24.1	13 11 29.187	−1 20 55.98	25.24	$2.63^{+0.48}_{-0.48}$	...	...
24.2	13 11 32.057	−1 19 50.33	24.80	$2.50^{+0.46}_{-0.46}$	...	...
24.3	13 11 30.295	−1 19 33.92	24.33	$2.43^{+0.45}_{-0.45}$	...	2.6
24.4	13 11 33.712	−1 20 19.75	24.99	$2.81^{+0.50}_{-0.69}$	...	...
26.1	13 11 25.146	−1 20 32.36	24.67	$1.08^{+0.39}_{-0.27}$	2.33±0.29	...
26.2	13 11 31.326	−1 20 25.16	25.39	$1.04^{+0.27}_{-0.27}$	...	...
26.3	13 11 30.245	−1 20 32.36	27.42	$0.77^{+2.53}_{-0.23}$	...	...
27.1	13 11 25.174	−1 20 33.11	25.22	$1.81^{+0.37}_{-0.37}$	2.38±0.28	...
27.2	13 11 31.366	−1 20 24.56	26.19	$1.58^{+0.48}_{-0.34}$	...	...
27.3	13 11 30.191	−1 20 32.76	29.82	$4.55^{+1.63}_{-0.73}$	...	...
28.1	13 11 28.298	−1 20 10.91	27.20	$1.17^{+4.29}_{-0.29}$	2.93±0.48	...
28.2	13 11 34.260	−1 21 00.01	26.47	$2.00^{+0.43}_{-1.23}$	...	...
29.1	13 11 29.240	−1 20 57.78	25.97	$2.47^{+0.57}_{-0.46}$	...	...
29.2	13 11 30.028	−1 19 33.92	25.00	$3.40^{+0.58}_{-0.58}$	...	...
29.3	13 11 32.164	−1 19 52.53	24.80	$2.50^{+0.46}_{-0.46}$	...	...
29.4	13 11 33.618	−1 20 20.55	25.84	$3.35^{+0.57}_{-0.57}$	...	2.5
30.1	13 11 32.424	−1 19 19.50	25.91	$4.49^{+0.72}_{-0.72}$	...	...
30.2	13 11 33.188	−1 19 25.81	25.80	$3.23^{+0.56}_{-0.76}$	...	...
30.3	13 11 33.662	−1 19 32.51	25.73	$3.30^{+0.56}_{-0.56}$	...	3.0
31.1	13 11 30.362	−01 19 51.13	23.77	...	...	1.8
31.2	13 11 33.271	−01 20 44.37	...	...	...	...
31.3	13 11 28.960	−01 21 10.19	25.37	...	...	...
31.4	13 11 26.504	−01 20 21.75	24.80	...	...	...
32.1	13 11 32.190	−01 20 03.34	...	...	...	...
32.2	13 11 33.218	−01 20 20.75	...	...	...	3.0
32.3	13 11 29.587	−01 21 02.49	...	...	...	...
32.4	13 11 29.801	−01 20 43.17	...	...	...	...
32.5	13 11 26.600	−01 19 57.60	...	...	...	3.0
33.1	13 11 28.440	−01 21 00.39	23.66	...	...	4.5
33.2	13 11 34.646	−01 20 33.56	26.62	...	...	...
35.1	13 11 28.493	−01 20 59.38	...	...	...	1.9
35.2	13 11 33.952	−01 20 33.36	...	...	...	...
35.3	13 11 29.427	−01 20 33.76	...	...	...	...
36.1	13 11 31.563	−01 19 45.73	...	...	...	3.0
36.2	13 11 31.683	−01 19 47.13	...	...	...	...
40.1	13 11 30.269	−01 20 11.43	...	...	...	2.5
40.2	13 11 26.174	−01 21 02.54	...	...	...	...

Table I. Multiple image systems considered in this work originating from Limousin et al. (2007).

The original units of right ascension were in hours, minutes, and seconds, while the units of declination were in degrees, arcminutes, and arcseconds. Using Microsoft Excel, we converted the image coordinates into map coordinates where both units of right ascension and declination were in degrees. We then subtracted the image center

from all of the coordinates and made the new coordinates, which were in degrees by now, the conversion is carried out by the process:

Right Ascension (hr/min/sec)	Declination (deg/arcmin/arcsec)
$X=((hr*15)+(min*15/60)+(sec*15/3600)-197.856)*3600$	$Y=((deg)+(arcmin/60)+(arcsec/3600)*cos((deg)+(arcmin/60)+(arcsec/3600))+1.327)*3600$

where (197.856, 1.327) is the image center position.

3.2 Pixelens

Below, we describe how we reconstructed the mass for Abell 1689. Schematically, we used the non-parametric method as implemented in the Pixelens software, which is publicly available for download online.[3]
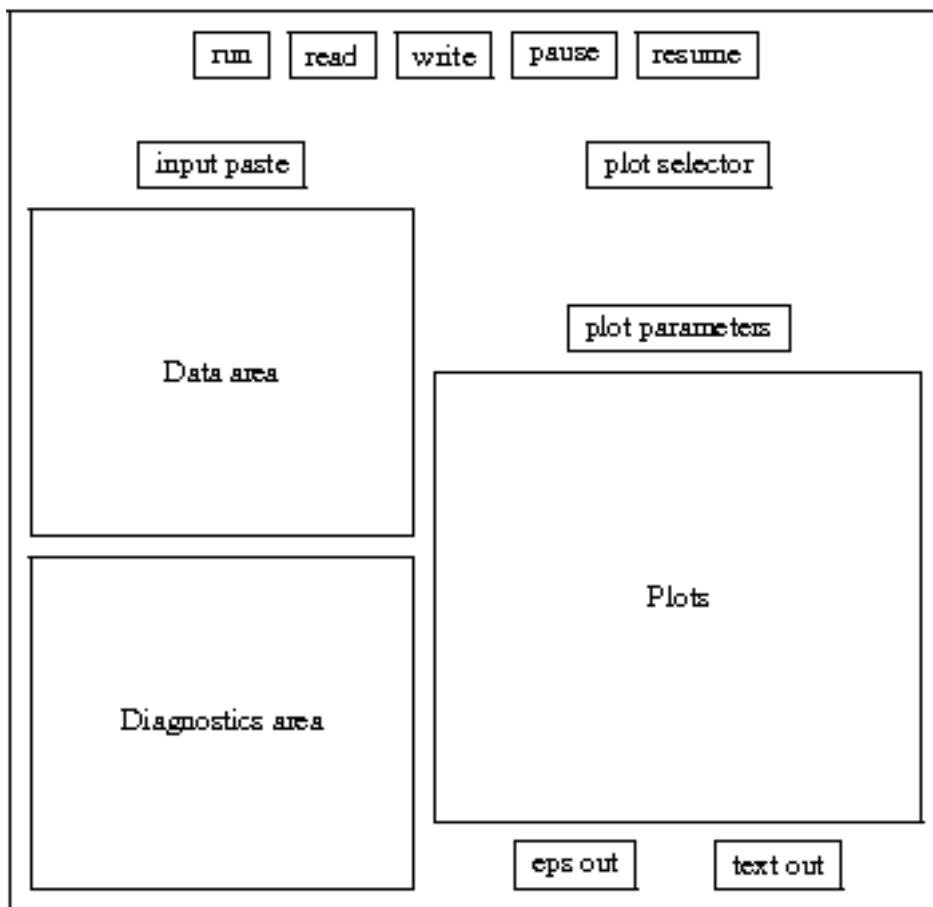
Figure 4. The graphical user interface for Pixelens.

3.2.1 What is Pixelens? How does Pixelens work?

Pixelens is a program written by Prasenjit Saha and Jonathan Coles for reconstructing gravitational lenses from multiple-image data. The program is based on Fermat's principle, which states that light will travel across the universe on extremal paths and gives gravitational lensing a geometric approach. An idea first used in Saha

---

[3] http://www.qgd.uzh.ch/programs/pixelens/

and Williams 1997 [3][4], Pixelens operates by reconstructing a pixilated mass map for the lens. (An example of the mass map is shown in Figure 5.) The advantage of using a pixilated mass map is that it allows for less complicated and faster calculations for non-parametric approaches. From the pixilated mass map, Pixelens is able to generate an ensemble of models, each of them a solution for the gravitational lensing.

We chose to use Pixelens for several reasons. For a massive cluster like A1689 that includes both smaller galaxy clusters and individual galaxies, Pixelens allows us to map out the distribution of mass on both scales and compare the distribution with theoretical predictions. Since the program is non-parametric, we can solve the lensing equation without constraints other than computational parameters that we enter into the program as inputs. Lastly, Pixelens was chosen because of its ability to generate any given number of model solutions consistent with the image positions, average out these solutions, and provide us with the best solution to the gravitational lensing problem, rather than a few mass maps.
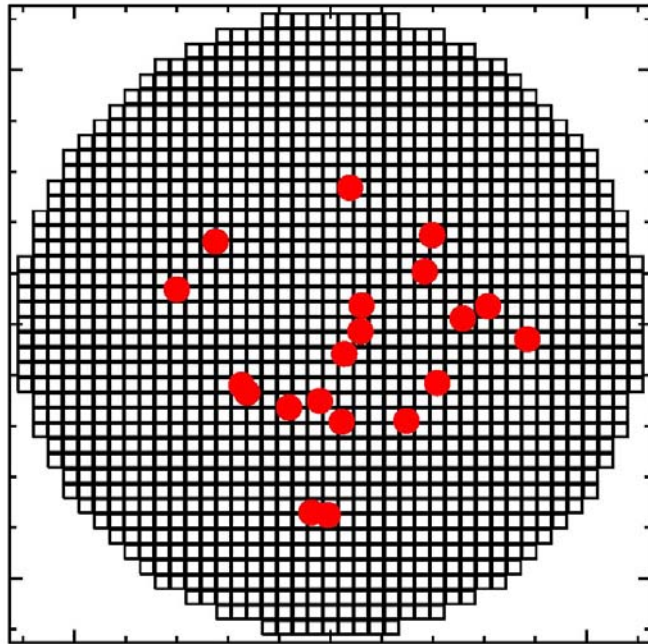
Figure 5. Example of pixilated mass map. Each of the squares is a mass pixel, and the images are marked in red.

3.2.2 What are the inputs/outputs?

The redshifts, pixel size, shear, steepness, details of the chosen prior, number of models, and image data are all model inputs that can go into the input area of the Pixelens graphical user interface. The compulsory constants we used were a radius of the mass map of 20 pixels and a lens redshift of z=0.18 for A1689. Optional constants

that we used included an external shear of 60 degrees, a model number of 50, a fixed Hubble age of g=14 (14 billion years), and a minimum steepness of zero.

Pixelens provides outputs in two ways. EPS, which is an image file, and DAT, which is a text file. Although the program offers a variety of output quantities, the main ones we looked at were the arrival times, mass contours (see Appendix B), enclosed mass, mass density, and potential (see Appendix C). The usage for each output we took notice of will be explained later on in the process of finding our Pixelens solution for A1689.

3.2.3   Finding solutions using Pixelens

In order for the data to be run by Pixelens, we first prepared the data from Table I by organizing the images into doubles, triples, quads, quints, and a hex (doubles have two images, triples have three, and so on). It is necessary for us to get the image arrival time order and parity right for Pixelens to run smoothly. The correct arrival time order was found by ordering the images according to decreasing radius using $x^2 + y^2$, where x and y are the right ascension and declination coordinates calculated previously. This arrival time criterion is only an approximate one, taking into account the second factor of two contributions to the light travel time. The first contribution comes from the geometric light path (refer to Figure 2) and the second from General Relativity where a light traveling through a gravitational potential well will take a longer time. The potential is deeper near the cluster center; therefore images will take a longer time to arrive. Thus we assume that images with greater $x^2 + y^2$ arrive earlier, as suggested by the Pixelens tutorial [5].

To check for the right parity, we plotted the arrival time surface from Pixelens' output. An example of the arrival time surface can be seen in Figure 4 below. The source is located at the center of the diagram. Images appear where the arrival-time surface has a maximum minimum, or saddle-point.
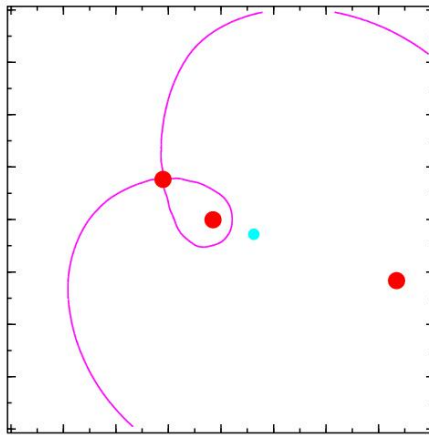

Figure 6. Arrival time surface for a triple with two minima (the two points that do not touch the contour line) and one saddle (the point that touches the contour line).

3.2.4 Running Pixelens

For mass determination, we chose to only use the doubles, quads, and quints to form combinations of images. For the nineteen different image combinations we ran, each had 20 images, composed of doubles, quads, and quints. In total, 11 sources were used, along with 38 images.

We ran each of the combinations, carefully observing the various outputs. The mass contours (see Appendix B) depicted the mass map of the images entered, and the enclosed mass and the surface mass density profiles were also shown. The latter depicts circularly averaged mass profiles. Units are 10^{12} M$_\odot$ for enclosed mass and 10^{12} M$_\odot$/kpc^2 for the surface density, against kpc. We then chose to extract the text outputs of the surface mass densities of each of the 19 combinations for curve fitting. The reason why we needed to do curve fitting was because only 21 data points were output for each combination, and the coordinates of the data points for different combinations were different. Although not used, we still retained the lens potentials in Appendix C for future reference.

3.3 GNUPLOT/ MATLAB curve fitting

We used Matlab to fit and plot the data points given by the Pixelens surface mass density text outputs. Matlab is a high-level language and interactive program that is able to quickly perform computationally rigorous tasks. Since there were nineteen 20-image combinations, there were 19 groups of data points sampled at different radii. We fitted each group with a 10th degree polynomial and then plotted the polynomial, as shown in Figure 7. We plotted all the polynomials together in Figure 8.
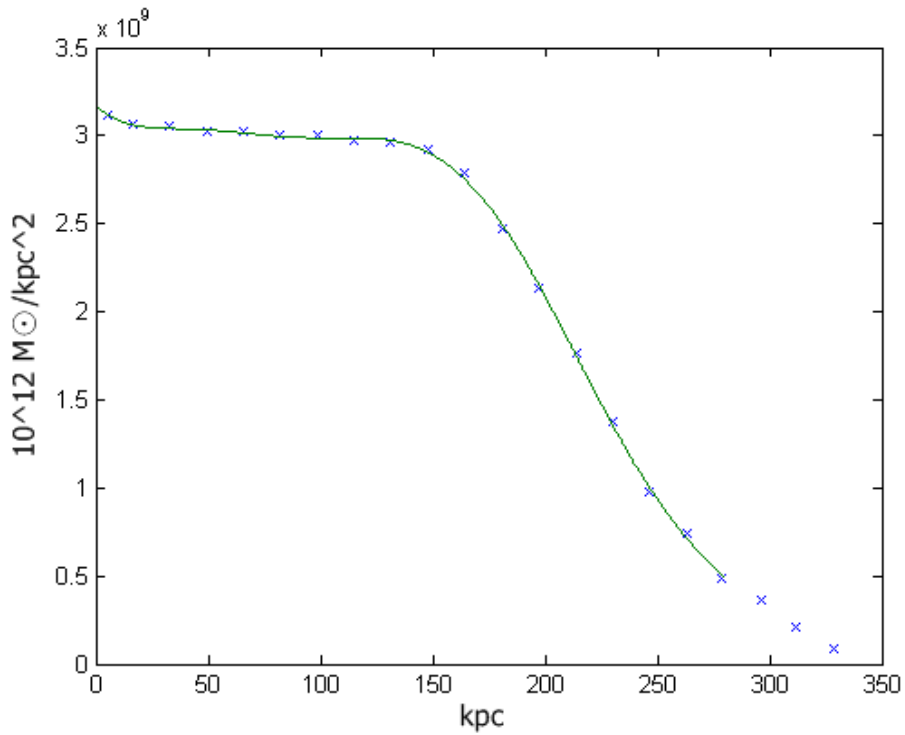
Figure 7. An example of using a 10th degree polynomial to fit the surface mass density coordinates. Units for the mass density are in 10^{12} M$_\odot$/kpc^2, against the radius in kpc.
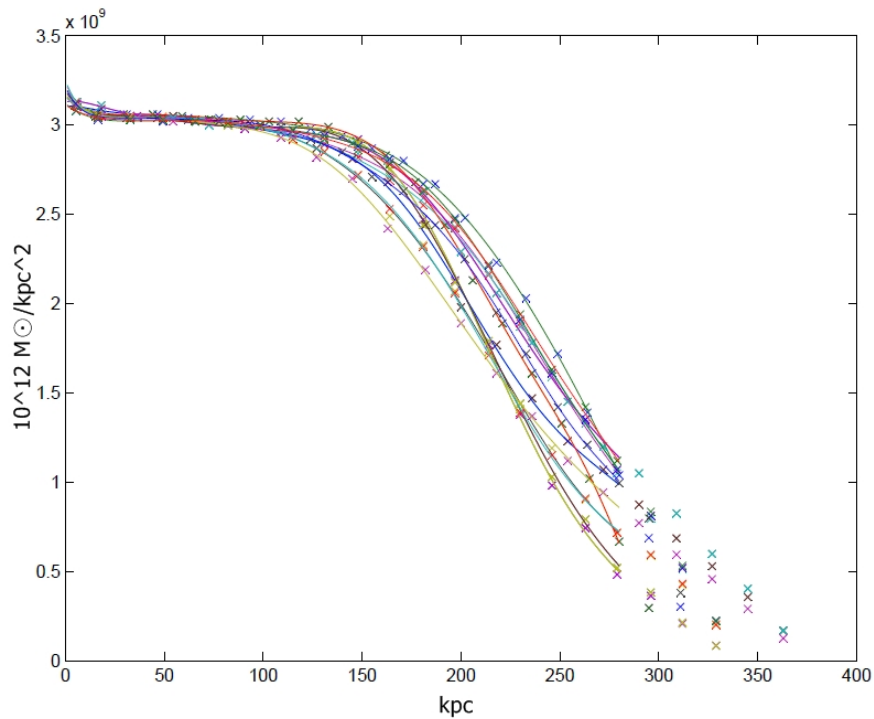

Figure 8. Diagram of all the 10th degree polynomials used to fit the 19 combinations. Units for the mass density are in 10^{12} M$_\odot$/kpc^2, against the radius in kpc.

3.4 Rebin

Taking the 10th degree polynomial fits shown in Figure 8, we rebinned the lines to do model fitting afterwards using Gnuplot. To rebin is to have a finite number of data points and rearrange those points in such a way that it is on one hand consistent with the original, and on the other hand more convenient for further manipulation. Gnuplot is a graphing utility used to visualize mathematical functions and data interactively. We used Gnufit, which is a nonlinear least squares fit program embedded in Gnuplot. The fit uses the Marquardt-Levenberg-algorithm (LMA) for fitting and the Gnuplot function evaluation mechanism for calculation.
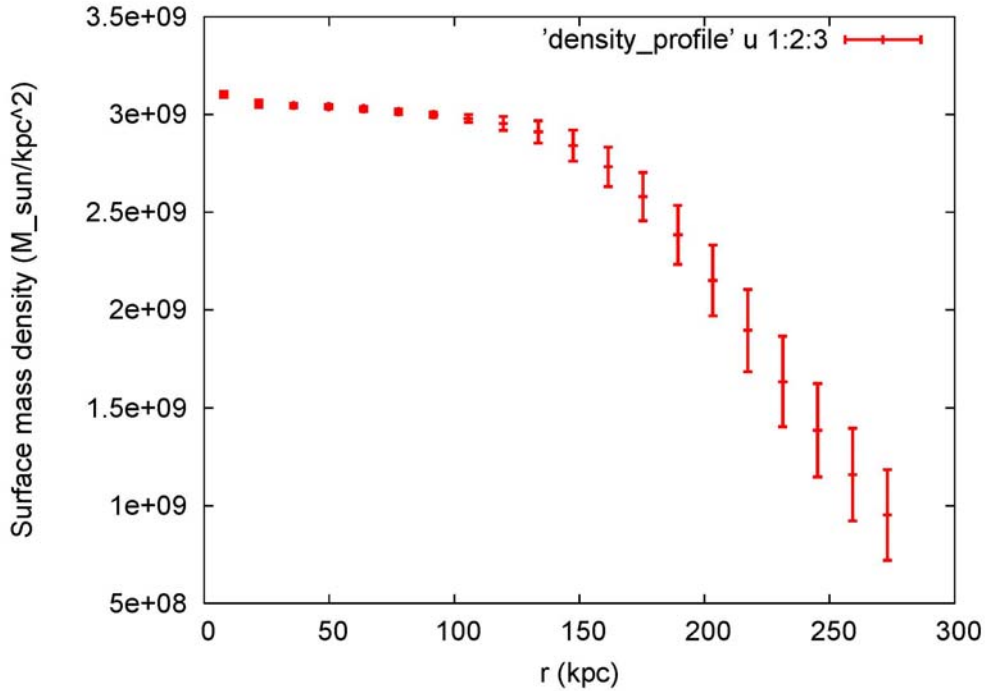
Figure 9. Rebin of the surface mass density in Figure 8.

4. RESULTS AND ANALYSIS

As a test for our lensing model, we checked the agreement of our result with various models, of which the equations, degrees of freedom (d.o.f.), chi-square, and asymptotic standard error are listed in Table II. The graphs of each profile fitting are also shown below. In Figures 10, 11 and 12, the rebin data are in red, and the best fit curve is in green.

Model	$\Sigma(r)$	(d.o.f)/ χ_ν^2 /asymptotic standard error
NFW	$\Sigma_{NFW}(r) = 2\kappa_s r_s f\left(\dfrac{r}{r_s}\right)$ $f(x) = \dfrac{1}{x^2-1}\left(1 - \dfrac{2}{\sqrt{x^2-1}}\arctan\sqrt{\dfrac{x-1}{x+1}}\right)$	(d.o.f)=18 χ_ν^2 =45.801 κ_s = 0.496341 (335.7%) r_s = 2.02458e+08 (314.8%)
Σ_1	$\Sigma_1(r) = \dfrac{a}{1+\left(\dfrac{r}{r_s}\right)^n}$	(d.o.f)=17 χ_ν^2 =1.38162 a= 3.04687e+09 (0.2083%) r_s = 243.097 (2.987%) n= 4.67887 (7.711%)
Σ_2	$\Sigma_2(r) = \dfrac{a}{1+\left(\dfrac{r}{r_s}\right)^n} + \dfrac{b}{r}$	(d.o.f)=16 χ_ν^2 =0.15671 a= 3.02146e+09 (0.09462%) r_s = 240.027 (0.9172%) n= 5.28304 (3.014%) b= 6.61988e+08 (8.49%)

Table II. The formulas for the three models we used for fitting, and their degrees of freedom (d.o.f.), chi-square in non-linear least square curve fitting in Gnuplot, and asymptotic standard error.
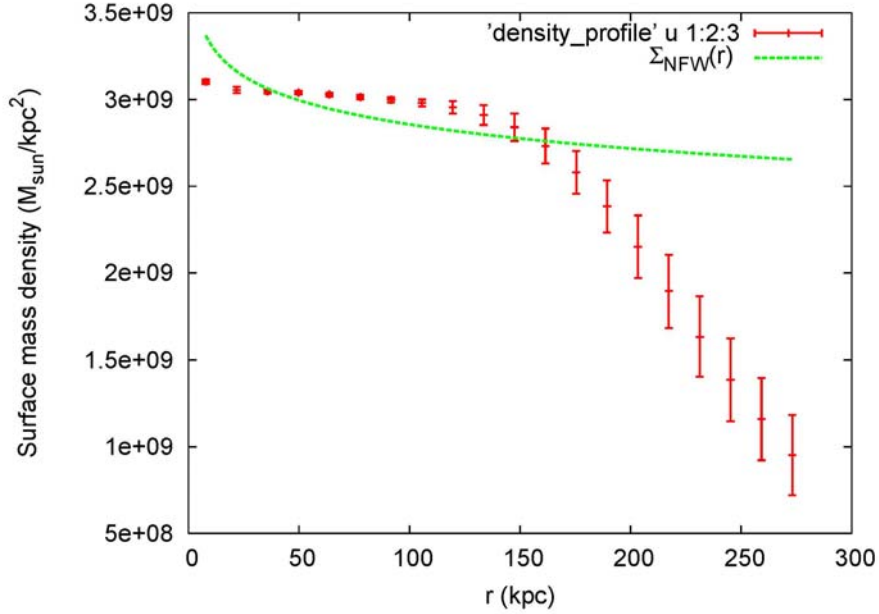

Figure 10. NFW profile fitting

We first tried to fit our data to the two-parameter NFW[4] profile (defined in Table II). Other works in the literature have been motivated to use NFW to fit their data

---

[4] Navarro, Frenk, and White (NFW [3]) universal profile of cold dark matter (CDM) halos.

because Cold Dark Matter (CDM) cosmology simulations often produce dark matter halos obeying the NFW profile. Our result (shown above in Figure 10) clearly does not follow NFW.
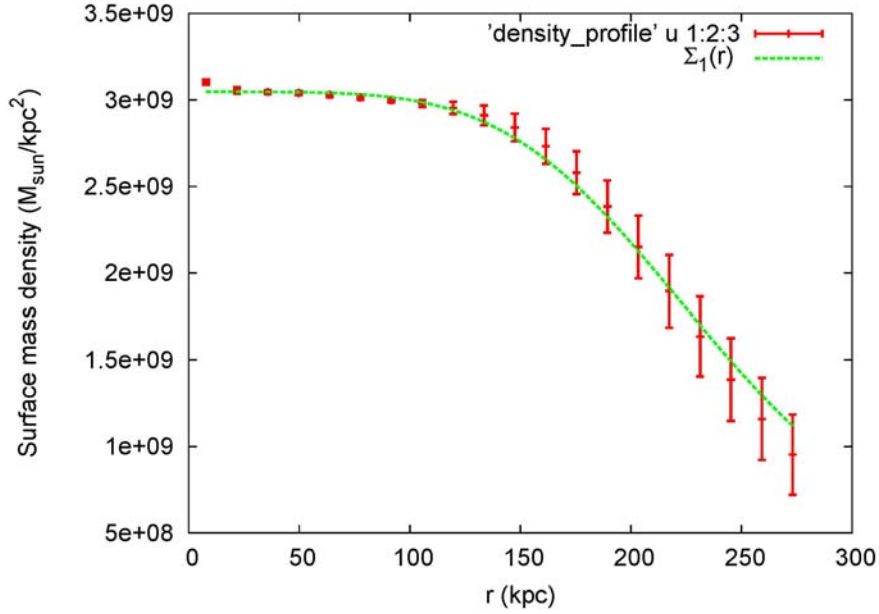

Figure 11. Σ_1 profile fitting.

Using a core model Σ_1 defined in Table II, we determined a best fit curve as shown in Figure 11. The data rules out the core model with 74.88% confidence. From the Σ_1 best fit curve we can see that the most distinct disagreement of the core model is at the inner most point, which rises above the line by 4 standard deviations. In order to improve the fit with the density profile data, we added a singular isothermal sphere (SIS) and refit our best curve (Figure 12). The SIS profile is often used as a solution to a self-gravitating system because of its simplicity.
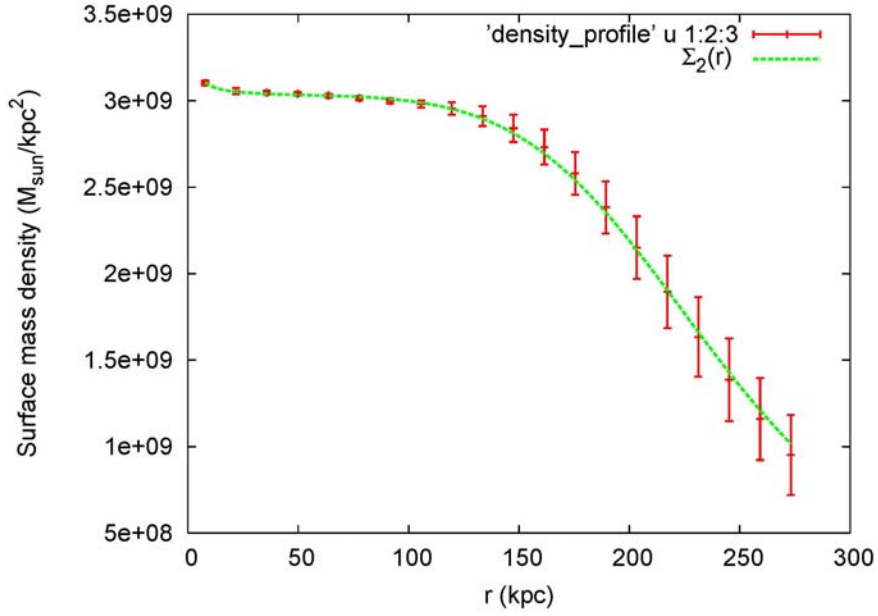
Figure 12. Σ_2 profile fitting.

By adding the SIS, we found that our model fit even better. The data agrees with the model at 85.50 % confidence. Therefore we have determined that the modified core model can best represent the data.
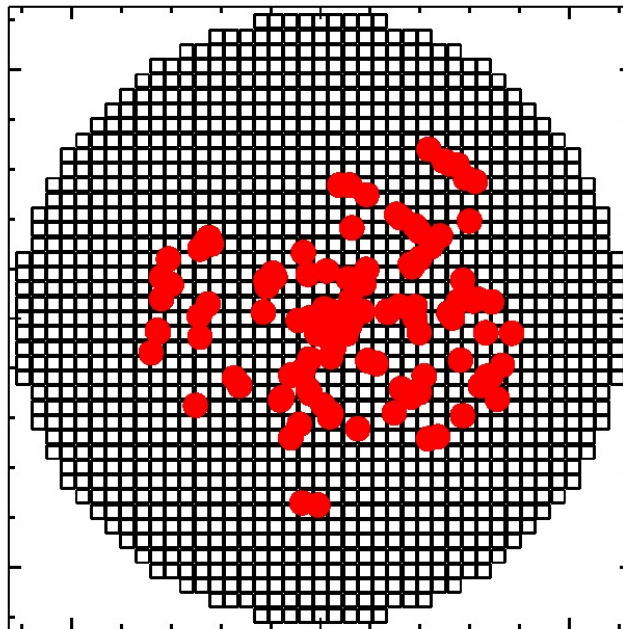

Figure 13. Pixelated mass map of all 34 sources and 110 images created using Pixelens. Here we notice that many of the images are close to the center.

5. CONCLUSION

Our work shows that the modified core model with a singular isothermal sphere agrees with the mass density profile created from the Pixelen's solutions. The core model fits our profile with a much higher level of confidence than that of the NFW model.

Prior works, such as Umetsu and Broadhurst (2008) [7], obtained results that agreed with the NFW mass model. They adopted a parametric approach to the strong lensing problem with limited parameters. The non-parametric approach we used allows for more degrees of freedom and therefore should provide more accurate solutions. Our result was very different from theirs. Below, we discuss possible causes of this discrepancy.

Out of the 34 sources with 110 images (see Figure 13) given by Limousin et al, only 11 sources and 38 images were actually used in our analyses. We found that Pixelens was unable to find solutions to combinations of sources with more than 20 images in total. The 19 combinations of 20 images we used were all chosen from the same 11 sources. Therefore, there is a strong sample bias with our limited use of data. Pixelens requires parity order of each image as part of the input. Image parity is a characteristic of an image located at the minimum, maximum or saddle of the arrive-time surface, and can be known only after, not before, the problem has been solved. Therefore it inevitably involves guesses, albeit educated guesses, and some parity orders are likely to be incorrect. This could be the main reason for the program's inability to find a solution to combinations of more images, leading to strong bias in our usable data.

In addition, we found that our solution yields an almost flat density core, in contrast to a sharply rising density core of the NFW model. Typically, a NFW model that has a central concentration of mass produces multiple images located at a distance, corresponding to the so-called Einstein radius, from the lens center. Near the lens center, images are demagnified and therefore less likely to be observable. However, our data shows that a relatively large fraction of images are located near the lens center. (See Appendix B of mass contour maps and Appendix C of potential contour maps in comparison with Fig.13.) This may be due to the sample bias in our selection of data and the reason why we obtained a very different lens mass profile that does not agree with the NFW model.

Finally, although Pixelens is an excellent program for solving gravitational lensing the non-parametric way and is popular for research in this area, it may be inadequate in finding solutions for extremely massive clusters like Abell 1689. Smaller galaxy clusters and individual galaxies, which produce only a few images, can be accurately solved by Pixelens. Abell 1689 may have too many sources and images for Pixelens to

handle all at the same time.

APPENDIX A
ANGULAR DIAMETER DISTANCE

Since the universe is in a state of expansion, there are many ways to measure distance in astronomy. Angular diameter distance is one of the ways. In the modern geometric model of our Universe, the angular diameter distance is a close approximation to the real distance when light leaves an object. The redshift z of an object is defined as the fractional Doppler shift of the light emitted by the object as it moves away from us. It is given by

$$z = \frac{v_e}{v_o} - 1 = \frac{\lambda_o}{\lambda_e} - 1,$$

where v_e and λ_e are the frequency and wavelength emitted and v_e and λ_e are the frequency and wavelength absorbed. Redshift is related to the scale factor of the universe since the wavelength of radiation scales linearly with the size of the expanding universe, so that

$$\frac{\lambda_o}{\lambda_e} = \frac{1}{a(t)} = 1 + z,$$

where $a(t_0) = 1$ and t is the time of emission of the radiation which we are looking back at. The Friedmann equation can be therefore written as

$$H(z) = H_0 \sqrt{\Omega_M (1+z)^3 + \Omega_\Lambda} = H_0 E(z),$$

where $E(z) \equiv \sqrt{\Omega_M (1+z)^3 + \Omega_\Lambda}$, Ω_k is the curvature density and H_0 is the Hubble parameter value.

Let us now define a set of commoving coordinates that remains constant as the universe expands. In these coordinates, the distance between any two objects at a time t is given by

$$d(t) = a(t)D_C = \frac{D_C}{1+z},$$

Where $d(t)$ is the proper distance, D_C is the constant commoving distance, and $a(t)$ is the scale factor. As the universe expands the proper distance changes. Since $a(t_0) = 1$, the commoving distance is the proper distance as measured today. By integrating over all the small distances along the trajectory of the light ray from the time of emission to the time of observation, we obtain the relation

$$D_C = \int_t^{t_0} \frac{cdt}{a(t)}.$$

The total line-of-sight commoving distance is therefore given

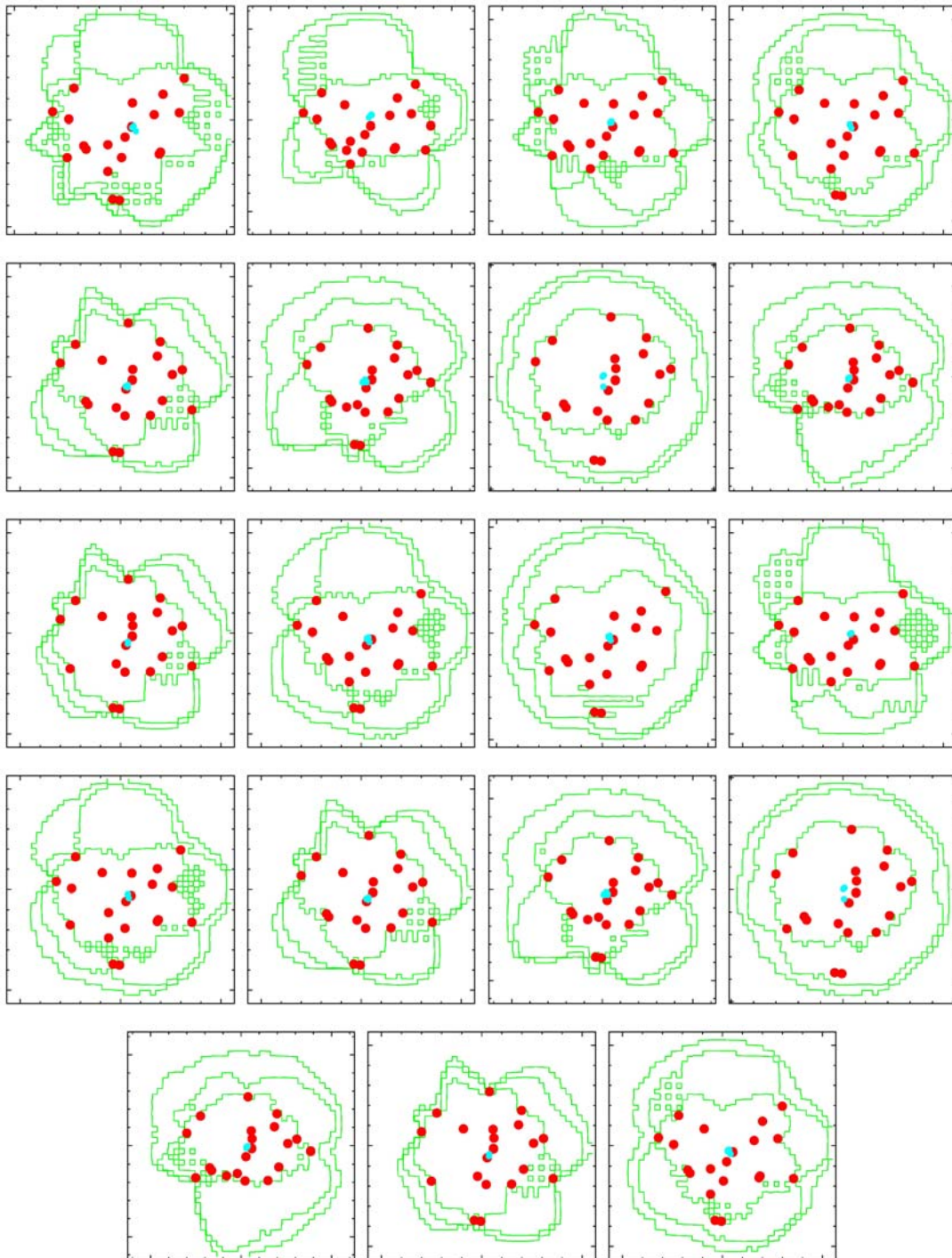$$D_C(z) = \frac{c}{H_0} \int_0^z \frac{dz'}{\sqrt{\Omega_M (1+z')^3 + \Omega_\Lambda}}.$$

The angular diameter distance D_A, which is defined as $D_A = \frac{D_C}{1+z}$, therefore can be written as

$$D_A(z) = \frac{D_C(z)}{1+z} = \frac{c}{H_0(1+z)} \int_0^z \frac{dz'}{\sqrt{\Omega_M (1+z')^3 + \Omega_\Lambda}}.$$

The angular diameter distance is the ration of an object's physical transverse size to its angular size (in radians).

APPENDIX B
MASS CONTOURS

The graphs here depict the mass contours of the 19 different combinations we used, generated by the Pixelens program. The mass contours, in units of the critical density, are in green, and the reconstructed sources are in cyan.

APPENDIX C
POTENTIAL
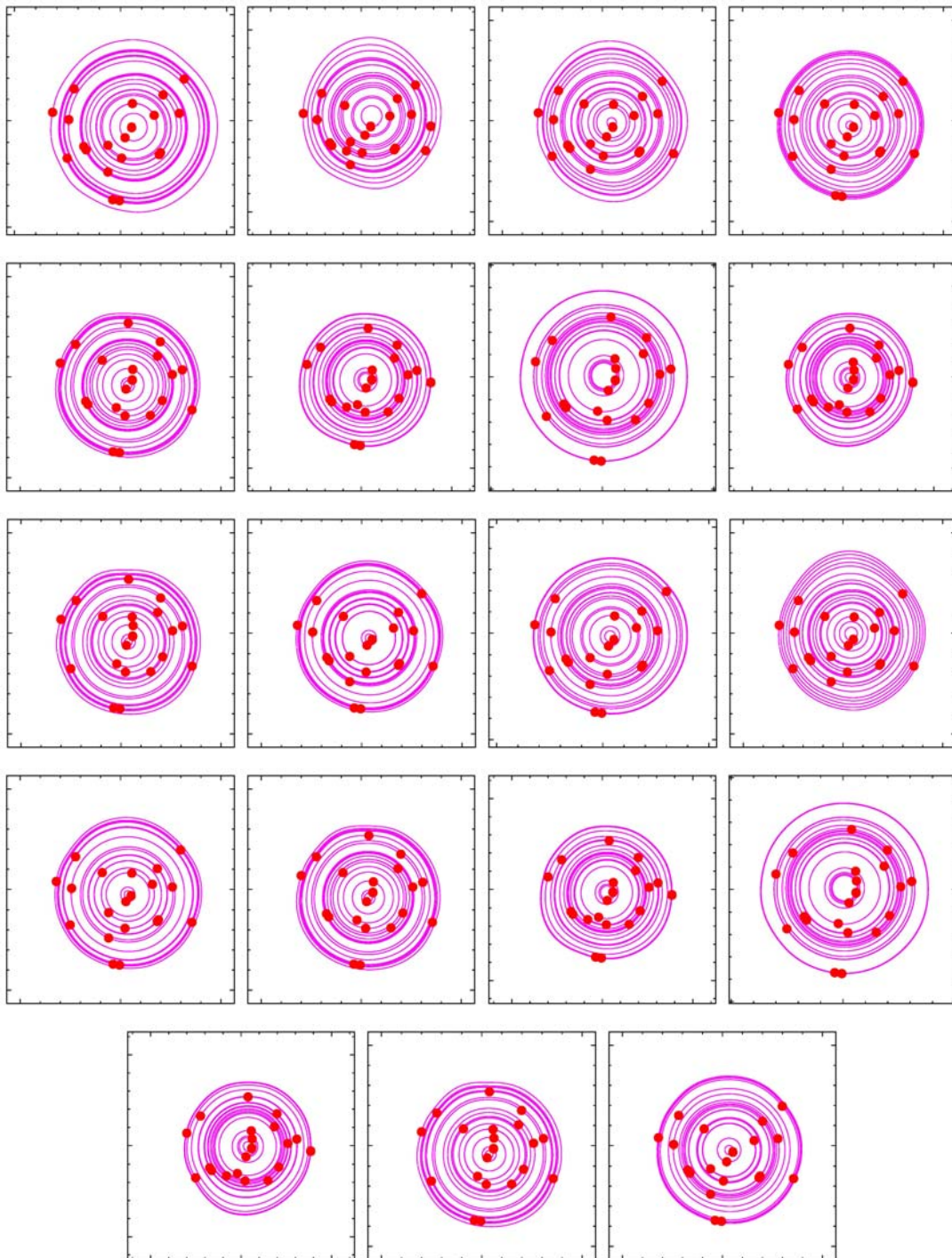
The graphs here depict the main lens potentials of the 19 different combinations we used, generated by the Pixelens program. The main lens potentials are attached for possible future use.

REFERENCES

[1] Schneider P., Kochanek C., and Wambganss J., *Gravitational Lensing: Strong, Weak and Micro,* Spinger (2005)

[2] Limousin M., Richard J., Jullo E., Kneib J., Fort B., Soucail G., Eliasdottir A., Natarajan P., Ellis R.S., Smail I., Czoske O., Smith G.P., Hudelot P., Bardeau S., Ebeling H., Egami E., Knudsen K.K., *ApJ*, 650-651 (2007)

[3] Saha P. and Williams L.L.R., *ApJ*, 148 (1997)

[4] Navarro J.F., Frenk C.S. and White S.D.M., *ApJ*, 490 (1997)

[5] Read J., *PixeLens Tutorial*, University of Zurich, Switzerland (2008)

[6] Read J., *PixeLens: Non-parametric lensing the Bayesian way*, University of Zurich, Switzerland (2008)

[7] Umetsu K. and Broadhurst T., *ApJ,* 177-203 (2008)